Contents lists available at ScienceDirect

Petroleum Science

Original Paper

# Development of an innovative permeability model for hydrate-bearing sediments under creep conditions: Effects of particle shape and non-uniform particle distribution

Yi-Han Shang [a,b], Gang Lei [a,b,*], Xiao-Yu Yuan [a,b], Ke-Yi Wang [a,b], Kai-Xuan Qiu [c,**]

[a] 511 62
[b] 3007
[c] 523808

ARTICLE INFO

Received 28 April 2025
Received in revised form
3 July 2025
Accepted 6 November 2025
Available online 13 November 2025

Edited by Teng Zhu

Hydrate-bearing sediments
Permeability
Creep
Non-uniform particle distribution
Particle shape
Hydrate pore morphology

ABSTRACT

Prolonged gas hydrate exploitation induces reservoir creep, leading to pore structure deformation, permeability reduction, and elevated risks of wellbore instability, ultimately impeding sustainable resource recovery. Accurate modeling of permeability evolution in hydrate-bearing sediments (HBS) under creep conditions is therefore crucial. However, the non-uniform distribution and irregular morphology of sediment particles complicate pore structures and fluid pathways, posing significant challenges for prediction. This study proposes a novel theoretical permeability model for HBS that incorporates the degree of non-uniform particle distribution, particle shape, pore structure creep, hydrate saturation, and hydrate pore morphology. Model validation against public datasets confirms its predictive capability. Sensitivity analysis reveals that pore structure creep, the degree of non-uniform particle distribution, and particle shape significantly influence permeability, with increased non-uniformity or larger particle aspect ratios leading to reduced permeability. For instance, after 40 h of creep, permeability decreases from 5 to 1.3 mD as the damage-related parameter $\beta$ increases from 0.4 to 1.0. The proposed model advances understanding of permeability evolution in HBS and provides a theoretical basis for the long-term development of natural gas hydrates.


## 1. Introduction

Natural gas hydrate (NGH) holds great potential as an alternative energy source, offering extensive reserves found primarily in marine sediments and permafrost regions

to be constant, and long-term hydrate extraction at this point triggers creep in hydrate-bearing sediments (HBS) (Li et al., 2019). Such creep compresses the pore spaces for fluid flow, resulting in reduced permeability and ultimately decreasing natural gas production (Chen et al., 2023; Hu et al., 2025). Therefore, understanding how creep affects permeability evolution in HBS is essential for sustainable and efficient NGH extraction. Since permeability not only characterizes the fluid flow capacity in HBS, but also reflects the complexity of the sediment's pore structure (Liu and Jeng, 2019;

* Corresponding author.
** Corresponding author.
- leigang@cug.edu.cn (G. Lei), qiukx@gbu.edu.cn (K.-X. Qiu).
Peer review under the responsibility of China University of Petroleum (Beijing).

Zhang et al., 2022), it is influenced by various factors under HBS creep (Ren et al., 2020). For example, the non-uniform distribution of sediment particles, which induces spatial variations in particle spacing (Bhade and Phirani, 2015; Liu et al., 2016), directly affects fluid flow capacity (Hafez et al., 2021) and thereby emerges as a key determinant of permeability (Peng et al., 2024). As permeability primarily depends on the geometric characteristics of the porous medium (Liu and Jeng, 2019), particle shape also can significantly influences fluid flow within the sediment (Tickell and Hiatt, 1938; Li et al., 2023; Song et al., 2024). Additionally, extensive triaxial creep experiments (Miyazaki et al., 2011, 2017; Li et al., 2019; Chen et al., 2023) have demonstrated that the effective stress greatly influences the mechanical behavior of HBS. Specifically, at low stress levels, the creep of HBS shows strong time dependence, and when the stress surpasses the sample's strength, HBS will directly collapse (Miyazaki et al., 2017). Other factors such as hydrate saturation (Wu et al., 2022; Zhang et al., 2022; Cheng et al., 2023) and hydrate pore morphology (Katagiri et al., 2017; Lv et al., 2021; Wang et al., 2021) also have non-negligible effects on permeability. Therefore, accurately predicting permeability changes requires a comprehensive consideration of these vital factors (i.e., the degree of non-uniform particle distribution, particle shape, pore structure creep, hydrate saturation, and hydrate pore morphology) on permeability of HBS.

Until now, many scholars have studied the relationship between hydrate saturation, hydrate pore morphology, and HBS permeability (Li et al., 2014; Mahabadi et al., 2019; Lv et al., 2021; Wang et al., 2021, 2025). To further study the fundamental mechanisms influencing the permeability of HBS, some experimental and theoretical studies have been carried out to explore the influence of the degree of non-uniform particle distribution (Peng et al., 2024), particle shape (Liu and Jeng, 2019; Yang and Chu, 2024), and pore structure creep on the permeability of HBS (Li et al., 2016, 2019; Cai et al., 2020; Wang et al., 2024). For example, based on Lattice Boltzmann method and Discrete Element method, Liu and Jeng (2019), Yang and Chu (2024) studied the impact of particle shape on HBS permeability, respectively. Li et al. (2024) proposed a permeability prediction model for complex geological conditions in the deep waters of the South China Sea using machine learning methods. Peng et al. (2024) developed a permeability model using vertical and horizontal particle distances to characterize the degree of non-uniform sediment particles. Their study suggest that non-uniform sediment particles distribution will significantly affect permeability of HBS. Although these studies can effectively study the impact of sediment particle shape and non-uniform distribution on permeability of HBS, they have not investigated the permeability of HBS under creep. Additionally, to better understand the permeability behavior of HBS under creep, Cai et al. (2020) conducted long-term water flow experiments on clay-silt sediment samples under stress conditions, and corroborated that the compression of pore and throat spaces in HBS accumulated as time increased. Besides experimental methods, theoretical models can also provide critical perspectives on the mechanisms of HBS permeability changes under creep effects (Lei et al., 2020; Li et al., 2022; Qu et al., 2025). For example, by combining a three-dimensional nonlinear creep constitutive equation and the KC equation, Zhang et al. (2020) proposed a fractional-order permeability model to characterize permeability of porous media at different creep stages. Recently, using nonlinear creep damage constitutive models (Liu et al., 2020; Hu et al., 2023; Sun et al., 2024), Lei et al. (2024a) and Qu et al. (2025) proposed permeability models to study the permeability change of HBS during creep. However, these theoretical models neglect the degree of non-uniform particle distribution (Kou et al., 2022; Song et al., 2024; Yang and Chu, 2024), and simplify sediment particles to spherical particles (Peng et al., 2024), which can introduce errors into permeability prediction. Thus, to more accurately predict the permeability behavior of HBS, more reliable permeability models should be established that incorporate creep, the non-uniform distribution and shape of sediment particles.

In this work, an innovative theoretical model is developed to predict HBS permeability under creep conditions, considering factors such as the degree of non-uniform particle distribution, particle shape, pore structure creep, hydrate saturation and hydrate pore morphology. Publicly available experimental results are used to verify the developed model. A parameter sensitivity analysis is then performed to assess the effect of key parameters (specifically, non-uniform parameter, particle aspect ratio, effective stress, dimensionless creep parameter and damage-related parameter) on permeability during creep. This derived model can precisely forecast HBS permeability evolution during long-term NGH extraction, providing theoretical support for mitigating wellbore instability risks, improving development efficiency, and optimizing extraction strategies.

## 2. Model development

### *2 1*

During the long-term extraction of NGH, stress loading causes time-dependent deformation of the sediment's pore structure (i.e., creep deformation) (Danesh et al., 2016; Guo et al., 2018). In this work, pore structures of HBS are characterized using the capillary bundle model (Fig. 1(a)) (Luo et al., 2023; Tang et al., 2024), which satisfy the fractal characteristics (Yu and Li, 2001; Yu and Cheng, 2002). The creep behavior of HBS is described by a nonlinear creep constitutive model (the details are shown in Fig. 2), in which the creep process is separated into three stages: decelerating creep, steady-state creep, and accelerating creep (Fig. 1(b)), where the emergence of accelerating creep marks the failure of HBS (Hu et al., 2023). This work focuses on grain-coating (GC) and pore-filling (PF) hydrates (Fig. 1(c)) in the pore space (Wang et al., 2021; Gao et al., 2024; Lei et al., 2024b; Tang et al., 2024). Additionally, the established permeability model complies with the following assumptions.

(1) Under triaxial stress conditions, the radial stresses are assumed to be equal (i.e., $\sigma_2 = \sigma_3$) (Miyazaki et al., 2017; Sun et al., 2024), and the stress is uniformly distributed (Lei et al., 2024b; Zhang et al., 2024). A two-dimensional Euclidean space is used to develop the model.
(2) Pore volume changes are due to the deformation of the skeleton and pores in HBS, with the deformation of sediment particles and hydrates neglected (Tang et al., 2023).
(3) The pore space contains only GC hydrate, PF hydrate, and their mixed morphologies (Wang et al., 2021; Gao et al., 2024). The phase transition of hydrates is quantified by the variation in hydrate saturation, while complex kinetic and thermodynamic behaviors are not considered (Qu et al., 2024).
(4) The sediment particles consist of ellipsoidal particles (Song et al., 2024), with their shape characterized by aspect ratio (Yang and Chu, 2024; Li et al., 2023). The degree of non-uniform distribution of particles in HBS is characterized by the non-uniform parameter (the ratio of the horizontal distance to the vertical distance between adjacent sediment particles) and the offset angle $\theta$ (i.e., the angle between the center line of two adjacent particles and the flow direction) (Peng et al., 2024). In addition, and $\theta$ remain constant during creep (Fig. 1(d)).

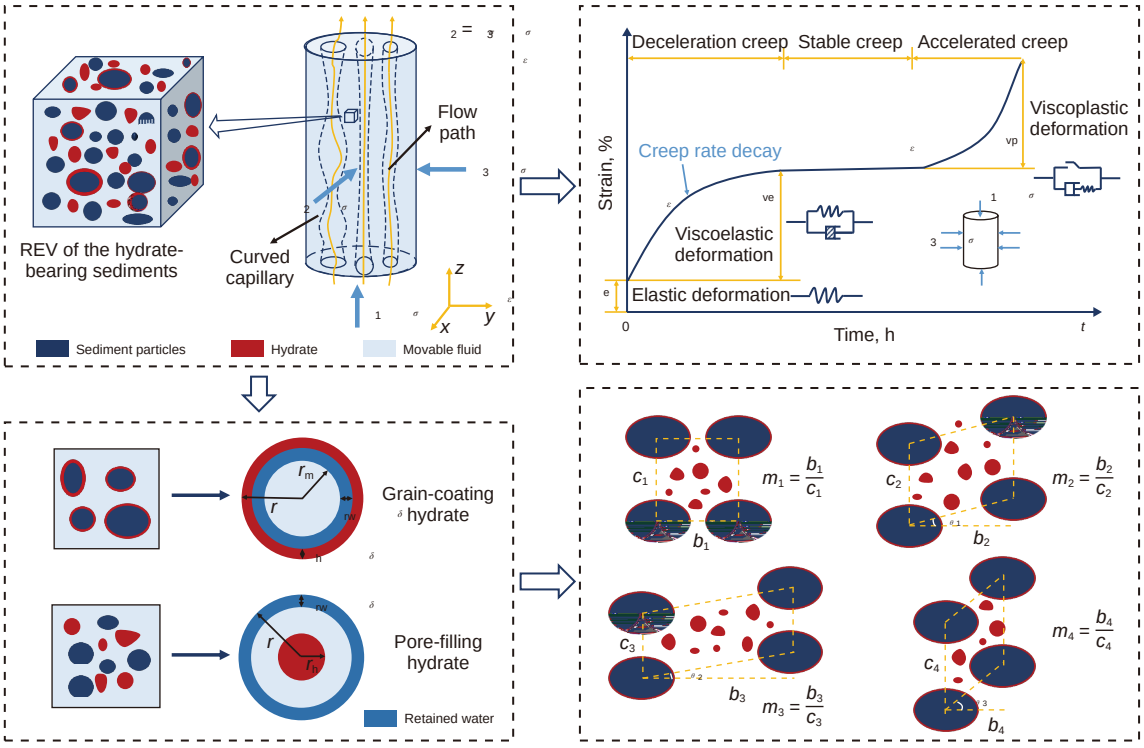


**Fig. 1.** Conceptual model of creep process of hydrate-bearing sediments under triaxial stress: **(a)** 3D structure of hydrate-bearing sediments; **(b)** General shape of creep curve of HBS sample; **(c)** Morphology of GC and PF hydrates; **(d)** Non-uniform distribution of sediment particles.

**Fig. 2.** Schematic of the nonlinear creep damage constitutive model of HBS.

*2 2*

The sediment skeleton consists of solid particles and hydrates (Lin et al., 2019), and provided the initial values of porosity $\varphi_0$ and hydrate saturation $_{h0}$ for HBS, the initial effective porosity $\varphi_e$ is determined by (Lei et al., 2020; Qu et al., 2024)

$$\varphi_e = \varphi_0(1 - {}_{h0}) \tag{1}$$

where $\varphi_0$ represents the initial porosity, $\varphi_e$ represents the initial effective porosity, $_{h0}$ represents the initial hydrate saturation.

During creep, due to the effects of axial stress $\sigma_1$, the second principal stress $\sigma_2$, and the third principal stress $\sigma_3$, the sediment skeleton deforms over time, leading to compression of the pore space (Li et al., 2019). Thus, the porosity of hydrate-free sediments under creep conditions can be derived by

$$\varphi = \frac{{}_p}{{}_b} = \frac{({}_{p0} - \Delta\ {}_p)/\ {}_{b0}}{({}_{b0} - \Delta\ {}_p)/\ {}_{b0}} = \frac{\varphi_0 - \varepsilon_v}{1 - \varepsilon_v} \tag{2}$$

where $_p$ and $_b$ represent the pore volume and apparent volume of HBS under creep conditions respectively, $_{p0}$ and $_{b0}$ are the initial pore volume and apparent volume respectively, $\Delta\ _p$ denotes the pore volume of change, $\varepsilon_v$ is the volumetric strain.

For HBS, the porosity under creep conditions can be determined by combining Eq. (1) and Eq. (2)

$$\varphi = \frac{\varphi_0(1 - {}_{h0}) - \varepsilon_v}{1 - \varepsilon_v} \tag{3}$$

Assuming the total volume of hydrates remains constant during creep (Qu et al., 2025), the hydrate saturation $_h$ under creep conditions is calculated by

$${}_h = \frac{{}_{p0}\ {}_{h0}}{{}_p} = \frac{{}_{p0}\ {}_{h0}}{{}_{p0} - \Delta\ {}_p} = \frac{{}_{h0}}{1 - \Delta\ {}_p/\ {}_{p0}} \tag{4}$$

where $\Delta\ _p/\ _{p0}$ can be determined by the following equation

$$\varphi = \frac{({}_{p0} - \Delta\ {}_p)/\ {}_{p0}}{({}_{b0} - \Delta\ {}_p)/\ {}_{p0}} = \frac{1 - \Delta\ {}_p/\ {}_{p0}}{1/\varphi_0 - \Delta\ {}_p/\ {}_{p0}} \square \frac{\Delta\ {}_p}{{}_{p0}} = \frac{1 - \varphi/\varphi_0}{1 - \varphi} \tag{5}$$

By substituting Eq. (5) into Eq. (4), the hydrate saturation $_h$ is expressed as

$$_{h} = \frac{\varphi_0(1-\varphi)\ _{h0}}{\varphi(1-\varphi_0)} \tag{6}$$

Hu et al. (2023) established a modified nonlinear creep damage constitutive model, derived from the Nishihara model (Yan et al., 2020), to accurately represent the creep behavior of HBS throughout the process. The modified model features a Hooke element, a Kelvin element and an ideal viscous element in series (Fig. 2), with the introduction of a nonlinear viscosity coefficient and an elastomer that takes into account the temporal damage to HBS, thereby describing the nonlinear creep characteristics of HBS. The steady-state creep stage is primarily governed by the Kelvin element, where $_1$ denotes its three-dimensional viscosity coefficient of the modified Kelvin element. When the axial load exceeds the long-term strength $\sigma_s$, accelerating creep occurs, causing permanent damage to the HBS. The accelerating creep stage is primarily characterized by the viscoplastic element, with $_2$ serving as the three-dimensional viscosity coefficient of the modified viscoplastic element.

According to the HBS creep model of Hu et al. (2023), the volumetric strain $\varepsilon_v$ under three-dimensional stress condition, where the second and third principal stresses are equal, can be described as

where $\sigma_1$, $\sigma_2$ and $\sigma_3$ are the axial stress, the second principal stress and the third principal stress, respectively; $_0$ is the shear modulus for the Hooke element in MPa, $_0$ is the bulk modulus for the Hooke element in MPa, $_1$ is the shear modulus of the modified Kelvin element in MPa, $_2$ is the shear modulus of the modified viscoplastic element in MPa, $_1$ is the three-dimensional viscosity coefficient of the modified Kelvin element in MPa□h, $_2$ is the three-dimensional viscosity coefficient of the modified viscoplastic element in MPa□h; and $\beta$ represent the dimensionless creep parameter, and the damage-related parameter, respectively; and $_1$ are the creep duration and the damage threshold time, respectively; $\sigma_s$ denotes the long-term strength.

Porosity $\varphi$, hydrate saturation $_h$, and volumetric strain $\varepsilon_v$ of HBS under creep conditions can be obtained by Eqs. (3), (6) and (7) respectively. Based on the fractal theory and Eq. (B1), the pore fractal dimension under creep conditions is $_f = 2 - (\ln \varphi)/\ln(\ _{min} / \ _{max})$. Assuming that the specific surface area of HBS stays unchanged dtions

comprehensively quantifying all hydrate morphologies is difficult. In addition, PF and GC hydrates are viewed as the two dominant hydrate growth patterns in HBS (Gao et al., 2024; Lei et al., 2024b; Qu et al., 2024; Tang et al., 2024). Therefore, this study primarily focuses on PF and GC hydrates, and the pore radius of HBS with GC and PF hydrates is determined by

$$\begin{cases} _{GC} = \sqrt{1 - _{h}} \\ _{PF} = \left(1 - \sqrt{_{h}}\right) \end{cases} \tag{12}$$

where $_{GC}$, $_{PF}$ are the pore radius with GC hydrate and PF hydrate respectively.

According to Hagen-Poiseuille theory (Washburn, 1921; Yu, 2008), the flow rate through a single pipe of diameter $\lambda$ is calculated by

$$_{-}(\lambda) = \frac{\pi}{128}\frac{\Delta}{_{t}}\frac{\lambda^4}{\mu} \tag{13}$$

where $_{-}$ is the flow rate through a single pipe, $\Delta$ is the pressure drop across the tube, $\lambda$ is the pore size of HBS, $\mu$ is the fluid dynamic viscosity, $_{t}$ is the actual length of the capillary, which can be calculated by Eq. (B3).

By adding up the flow rate from each pipe by combining Eq. (13) and Eq. (B5), the total flow through the REV cross-section of HBS with GC and PF hydrates can be determined by

$$\begin{cases} Q_{GC} = -\int_{\lambda_{min}\sqrt{1-_{h}}}^{\lambda_{max}\sqrt{1-_{h}}} {}_{-}(\lambda)\mathrm{d}\lambda = \left\{ \dfrac{\frac{\pi}{128}\frac{\Delta}{\mu}\frac{2-_{T}}{0}\left(\lambda_{max}\sqrt{1-_{h}}\right)^{3+_{T}}}{\left[1-\left(\frac{\lambda_{min}}{\lambda_{max}}\right)^{3+_{T}-_{f}}\right]} \right\} \\ Q_{PF} = -\int_{\lambda_{min}\left(1-\sqrt{_{h}}\right)}^{\lambda_{max}\left(1-\sqrt{_{h}}\right)} {}_{-}(\lambda)\mathrm{d}\lambda = \left\{ \dfrac{\frac{\pi}{128}\frac{\Delta}{\mu}\frac{2-_{T}}{0}\left[\lambda_{max}\left(1-\sqrt{_{h}}\right)\right]^{3+_{T}}}{\left[1-\left(\frac{\lambda_{min}}{\lambda_{max}}\right)^{3+_{T}-_{f}}\right]} \right\} \end{cases} \tag{14}$$

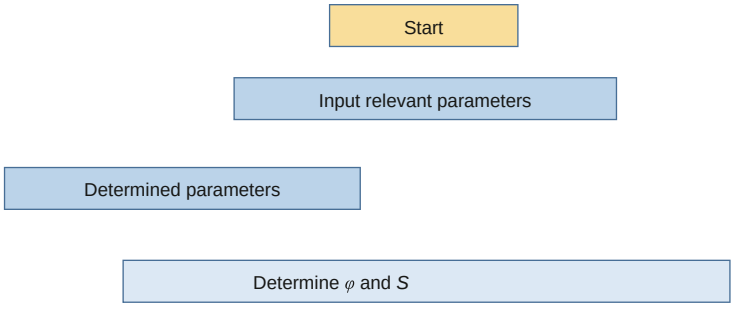


**Fig. 3.** Workflow of the proposed permeability model.

where $Q_{GC}$ and $Q_{PF}$ are the total flow through the REV cross-section of HBS with GC and PF hydrates respectively, $_T$ is the tortuosity fractal dimension, which can be obtained by Eq. (B2). Due to the Euclidean dimension is 2 in this work, we have $1 < _T < 2$, and $1 < _f < 2$ (Yu and Cheng, 2002). As mentioned before, $\lambda_{min}/\lambda_{max} = 0.01$, Eq. (14) can be simplified to

According to Darcy's law (Lei et al., 2020), the permeability of HBS with GC and PF hydrates is given by

$$\begin{cases} _{GC} = \dfrac{\mu \ _0 Q_{GC}}{\Delta P A} = \dfrac{\pi}{128} \dfrac{^{1-\ _T}}{} \dfrac{_f}{3 + \ _T - \ _f} \left(\lambda_{max} \sqrt{1 - \ _h}\right)^T \end{cases}$$

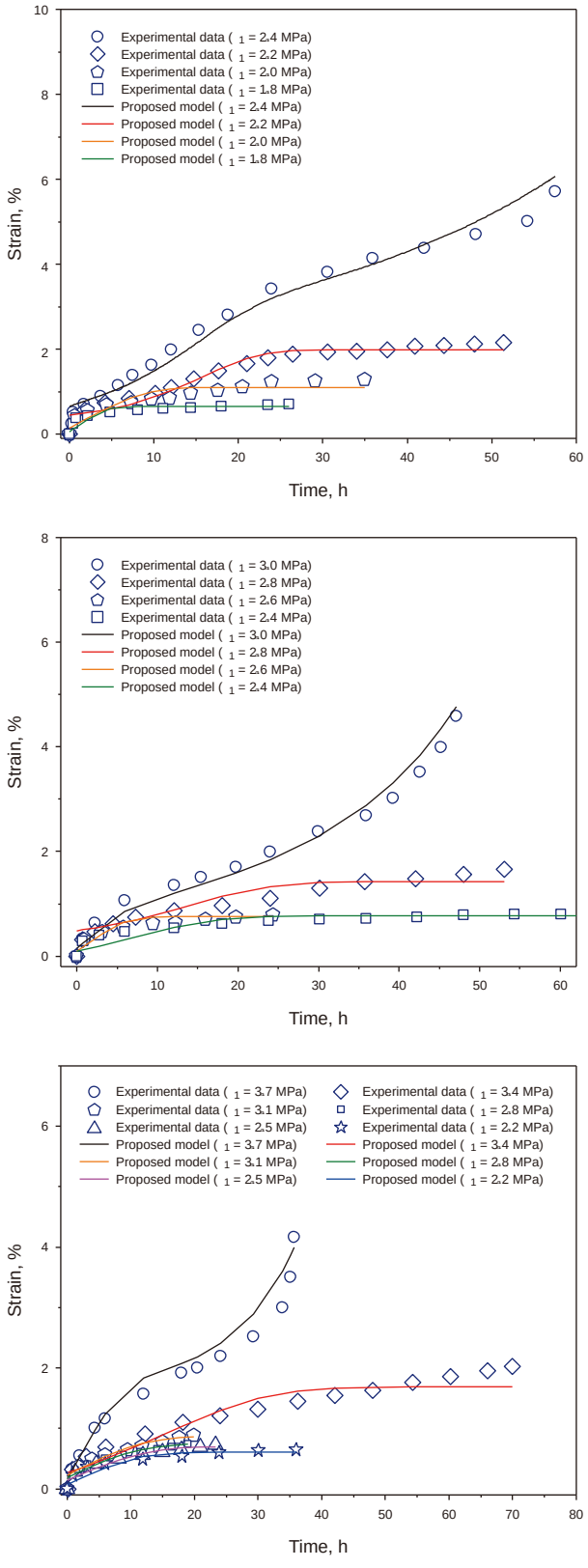


**Fig. 4.** Comparison of predicted strains with experimental data under different stresses and initial hydrate saturation: **(a)** $_{h0} = 20\%$; **(b)** $_{h0} = 30\%$; **(c)** $_{h0} = 40\%$.

sediment framework, thereby enhancing its rigidity and strength (Qu et al., 2024; Wang et al., 2025).

*312*

The proposed model's predicted permeability is assessed in comparison with experimental data from Cai et al. (2020) (Fig. 5). By conducting the seepage experiments on HBS samples from gas hydrate reservoirs in the Shenhu area of the South China Sea, Cai et al. (2020) investigated the fundamental mechanism behind permeability change of HBS under creep. In the modeling setup, the reasonable range of the parameter values is obtained from Hu et al. (2023) and Wang et al. (2021), as shown in Table 4. Other key parameters are set as follows: $\varphi_0 = 0.33$, $_{h0} = 31\%$, $= 0.2$, $\theta = \pi/9$, $\alpha = 0.8$, $_1 = 60$ h, $= -6.06 \times 10^{-2}$, and $\beta = 3.94$. As illustrated in Fig. 5(a), the porosity predicted by our model matches well with the test data. In addition, Fig. 5(a) and (b) indicate that, when the axial stress increases from 10 to 100 kPa, porosity decreases from 18.6% to 11.2%, and permeability decreases from 13.44 to 3.51 mD. Moreover, Fig. 5(b) demonstrates that during the creep process, even under a constant axial stress, the permeability decreases continuously over time. Table 4 shows that the value of parameter $\eta$ rises over time, indicating that during creep, the GC hydrate transitions to PF hydrate in HBS. The compression of the pore space in HBS under creep conditions (Zhong et al., 2020) may be the main factor, causing an increase in hydrate saturation (Qu et al., 2025). Essentially, as hydrate saturation increases, gas hydrates tend to occur predominantly at the center of the pores (Zhang et al., 2024).

To further validate the accuracy of our proposed model, experimental permeability data from Lu et al. (2019) are compared with the calculated permeability results from the derived model (Fig. 6). To study the evolution of permeability in hydrate-bearing clayey-silt sediment during gas hydrate exploitation via depressurization, Lu et al. (2019) conducted four groups of water seepage experiments under various stress conditions: (I) for the first seepage experiment, $\sigma_1 = 20, 60, 80, 90, 100, 150, 200$ kPa; (II) for the second seepage experiment, $\sigma_1 = 20, 60, 80, 90, 100$ kPa; (III) for the third experiment, $\sigma_1 = 10, 30, 40, 50$ kPa; (IV) for the fourth experiment, $\sigma_1 = 10, 30, 50, 75, 100$ kPa, corresponding to Fig. 6(a)–(d), respectively. The stress loading conditions are adjusted to correspond with the axial stress applied in the experiment during the modeling procedure. The model parameters are set as follows: $\varphi_0 = 0.33$, $_{h0} = 31\%$, $= 0.2$, $\theta = \pi/9$, $\alpha = 0.8$, and $_1 = 60$ h, with additional parameters detailed in Table 5. As depicted in Fig. 6, the predicted permeability does not closely align with the experimental permeability during the early period (0–1200 min), whereas they align well in the later period. Fluctuations in the experimental instruments during the early measurements are responsible for the discrepancy in the initial period. Overall, the proposed model successfully captures the permeability evolution of HBS under creep conditions. Consistent with the results in Figs. 5 and 6 shows that permeability decreases over time even under constant stress. The value of parameter $\eta$ in Table 5 also illustrates that the hydrate pore morphology changes from GC to PF under creep.

To validate the applicability of the proposed model for predicting the permeability of gas hydrate-bearing sediments in permafrost regions, experimental permeability data from Chuvilin et al. (2025) are compared with the permeability calculated by Eq. (17) (Fig. 7). Chuvilin et al. (2025) measured the gas permeability

**Table 1**
Parameters for the model validation in Fig. 4(a).

| Parameters | [a] = 1.8 MPa | [a] = 2.0 MPa | [a] = 2.2 MPa | [a] = 2.4 MPa |
|---|---|---|---|---|
| $\sigma_s$[a], MPa | 2.2 | | | |
| $_0$[b], MPa | 2489 | 689 | 2489 | 2489 |
| $_0$[b], MPa | 580 | 480 | 58 | 58 |
| $_1$[b], MPa | 100 | 70 | 48 | 48 |
| $_2$[b], MPa | 40 | 40 | 60 | 40 |
| $_1$[b], MPa□h | 42 | 15 | 78 | 78 |
| $_2$[b], MPa□h | 250 | 250 | 250 | 250 |
| [b] | 0.3 | 0.15 | 0.15 | 0.15 |
| $\beta$[b] | 1.85 | 1.85 | 1.85 | 1.85 |

[a] These values are obtained from Sun et al. (2024).
[b] The acceptable range of these values are obtained from Hu et al. (2023).

**Table 2**
Parameters for the model validation in Fig. 4(b).

| Parameters | [a] = 2.4 MPa | [a] = 2.6 MPa | [a] = 2.8 MPa | [a] = 3.0 MPa |
|---|---|---|---|---|
| $\sigma_s$[a], MPa | 2.8 | | | |
| $_0$[b], MPa | 2489 | 2489 | 3489 | 2489 |
| $_0$[b], MPa | 480 | 580 | 68 | 580 |
| $_1$[b], MPa | 118 | 130 | 100 | 180 |
| $_2$[b], MPa | 100 | 100 | 100 | 120 |
| $_1$[b], MPa□h | 18 | 40 | 42 | 82 |
| $_2$[b], MPa□h | 250 | 250 | 250 | 200 |
| [b] | 0.09 | 0.22 | 0.1 | 0.25 |
| $\beta$[b] | 1.85 | 1.85 | 1.85 | 3.25 |

[a] These values are obtained from Sun et al. (2024).
[b] The acceptable range of these values are obtained from Hu et al. (2023).

of gas hydrate-bearing sediment samples from permafrost regions under different axial pressures ($\sigma_1$ = 4, 5, 6, 7, 8, 9, 10 MPa). To be consistent with the experiment, the parameters are set as follows: $\varphi_0 = 0.37$, $_{h0} = 51\%$, $= 0.2$, $\theta = \pi/9$ and $\alpha = 0.8$. As can be seen from Fig. 7, the predicted results generally fit well with the experimental data. However, when the axial pressure increases from 6 to 7 MPa, the permeability measured in the experiment drops suddenly, and there is a deviation between the prediction result and the experimental data. A possible reason is that before this axial stress range, the reduction in permeability is caused by the compression of pore space due to effective stress, while at this moment, the phase equilibrium in the pore structure is broken, and the decomposition of hydrates in the pore structure leads to a sudden change in the pore space structure (Chuvilin et al., 2025).

### 3.2

In this part, to deepen the understanding of the proposed model and supply a theoretical foundation for NGH extraction, a parameter sensitivity analysis is performed to evaluate the effect of key parameters (e.g., $_{h0}$, $\sigma_1$, , $\alpha$, , and $\beta$) on creep strain and permeability of HBS under creep conditions. During the modeling process, the relevant input parameters are set based on Fig. 6(a). Specifically, these parameters are as follows: $\varphi_0 = 0.33$, $_{h0} = 31\%$, $_{max0} = 5.95$ μm, $= 0.2$, $\theta = \pi/9$, $\alpha = 0.8$, $_1 = 40$ h, $= -6.06 \times 10^{-2}$, $\beta = 3.94$, $\gamma = 0.3$, and $\eta = -1.6$. As illustrated in Fig. 8, the initial hydrate saturation significantly affects both creep strain and permeability. Specifically, a higher initial hydrate saturation leads to a smaller creep strain (Fig. 8(a)). This indicates a clear inverse correlation between initial hydrate saturation and creep strain. This phenomenon can be mechanistically explained by the load-bearing capacity of hydrates within the HBS. As hydrate saturation increases, the hydrate phase assumes a greater proportion of the external load, effectively reinforcing the sediment skeleton (Wu et al., 2023). This reinforcement mechanism enhances the overall stiffness of the sediment system, consequently suppressing creep deformation through improved structural resistance to time-dependent strain. In addition, during HBS creep process, a lower initial hydrate saturation leads to a higher initial permeability and a greater reduction in permeability (Fig. 8(b)). For example, for the HBS with $_{h0} = 20\%$, the permeability decreases by 24.9% when the time increases from 0 to 40 h, while the permeability with $_{h0} = 40\%$ decreases by 23.0% within the same time period. The possible reason is that, at lower hydrate saturation, a substantial proportion of pore spaces remain unoccupied, creating more compressible pore spaces in HBS, which in turn causes a more significant reduction in permeability (Yoshimoto and Kimoto, 2022).

Fig. 9 illustrates the impact of ellipsoidal particle aspect ratio $\alpha$, non-uniform parameter , dimensionless creep parameter , related damage parameter $\beta$, and axial stress $\sigma_1$ on permeability of HBS during creep. As shown in Fig. 9(a), the smaller the aspect ratio of the ellipsoidal sediment particles, the larger the permeability of HBS (when $\alpha$ increases from 0.4 to 1.6, the predicted permeability calculated by Eq. (17) decreases from 33.5 to 18.3 mD in the initial stage of creep). This indicates that, along the flow direction, the permeability of sediments composed of transverse ellipsoidal particles ($\alpha < 1$) is greater than that of longitudinal ellipsoidal particles ($\alpha > 1$). This is because transverse ellipsoidal particles facilitate a looser particle arrangement, creating larger pore spaces and thus higher permeability. Moreover, the smaller aspect ratio $\alpha$ results in a longer $_1$ of ellipsoidal particles, forming straighter seepage channels that reduce tortuosity and tortuosity fractal dimension, thereby increasing seepage flow (Xiong et al., 2025). In contrast, longitudinal ellipsoidal particles experience a stacking effect, arranging more tightly, which results in smaller pore space and lower permeability (Song et al., 2024). The relationship illustrated in Fig. 9(b) shows that the smaller the non-uniform parameter , the more non-uniform the distribution of sediment particles, resulting in a reduced permeability of HBS

**Table 3**
Parameters for the model validation in Fig. 4(c).

| Parameters | [a] = 2.2 MPa | [a] = 2.5 MPa | [a] = 2.8 MPa | [a] = 3.1 MPa | [a] = 3.4 MPa | [a] = 3.7 MPa |
|---|---|---|---|---|---|---|
| $\sigma_s$[a], MPa | 3.4 | | | | | |
| $_0$[b], MPa | 2489 | 2489 | 2489 | 2489 | 2489 | 2489 |
| $_0$[b], MPa | 650 | 250 | 200 | 190 | 190 | 170 |
| $_1$[b], MPa | 135 | 150 | 169 | 160 | 160 | 80 |
| $_2$[b], MPa | 100 | 100 | 100 | 100 | 100 | 100 |
| $_1$[b], MPa□h | 12 | 12 | 12 | 12 | 12 | 12 |
| $_2$[b], MPa□h | 250 | 250 | 250 | 250 | 250 | 250 |
| [b] | 0.08 | 0.08 | 0.08 | 0.08 | 0.08 | 0.06 |
| $\beta$[b] | 1.85 | 1.85 | 1.85 | 1.85 | 1.85 | 1.85 |

[a] These values are obtained from Sun et al. (2024).
[b] The acceptable range of these values are obtained from Hu et al. (2023).

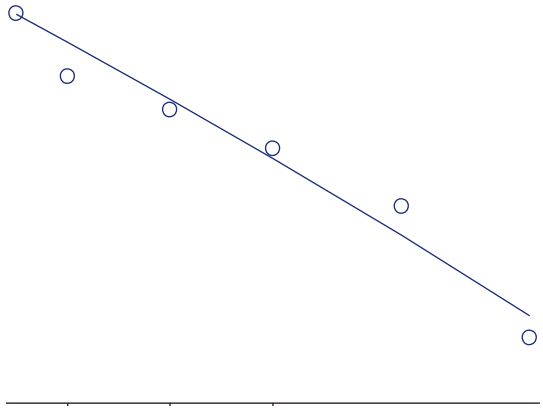

**Fig. 5.** Comparison of predicted porosity and permeability with experimental data under different stresses ($\sigma_1$ = 10, 30, 50, 75, 100 kPa): **(a)** Porosity; **(b)** Permeability.

(when increases from 0.1 to 0.8, the predicted permeability increases from 13.4 to 80.4 mD in the initial stage of creep). Additionally, at the same creep time, the closer is to unit, the greater the increase in permeability. This demonstrates that the non-uniform distribution of sediment particles plays a crucial role in the permeability of HBS. As indicated in Fig. 9(c), during the creep-stable stage (2–34 h), the permeability of HBS is strongly influenced by the dimensionless creep parameter , with permeability decreasing as the value of parameter increases. This is due to the fact that, the parameter in the Kelvin unit of the proposed model indicates the pore structure deformation of HBS during the creep-stable stage. In general, a higher value of parameter is associated with a greater deformation in the creep-stable stage. Thus, parameter and the permeability of HBS are negatively related during the creep-stable stage. Similarly, the accelerated creep stage is governed by viscoplastic deformation, characterized by the damage parameter $\beta$. In essence, a larger value of parameter $\beta$ implies a greater pore structure damage of HBS during the acceleration creep stage (17–40 h), resulting in a smaller permeability (Fig. 9(d)). For instance, for a given creep time 40 h, the permeability of HBS decreases from 4.9 to 1.3 mD when the damage parameter $\beta$ varies from 0.4 to unit. Fig. 9(e) shows that as axial stress increases, the compression of pore space contributes to a reduction in permeability. This reduction becomes more pronounced as the creep time increases, which is expected. For example, when = 40 h, the permeability of HBS decreases from 17.1 to 0.4 mD when the axial stress $\sigma_1$ varies from 0.4 to 1 2 MPa Fig. 9(f) presents a two-factor sensitivity analysis of the aspect ratio $\alpha$ of sediment particles and the non-uniform parameter . Generally, larger values of and smaller particle aspect ratio $\alpha$ increase the permeability of the HBS. When the aspect ratio of ellipsoidal particles changes, the extent of permeability reduction corresponding to different values varies. Specifically, when = 0.4, as $\alpha$ changes from 0.4 to 1.4, the permeability decreases by 90.5%; when = 0.1, as $\alpha$ changes from 0.4 to 1.4, the permeability decreases by 31.9%. At the same particle aspect ratio, increasing the value of can significantly increase the permeability. For example, when $\alpha$ = 0.4, as changes from 0.1 to 0.2, the permeability increases from 16.9 to 31.5 mD, and as changes from 0.1 to 0.4, the permeability increases from 16.9 to 221.3 mD. This demonstrates the coupled effect of the aspect ratio $\alpha$ and the non-uniform parameter on permeability.

Based on the above sensitivity analysis, it can be seen that the particle aspect ratio $\alpha$, non-uniform parameter , dimensionless creep parameter , related damage parameter $\beta$, axial stress $\sigma_1$, and creep time have significant effects on the permeability of HBS

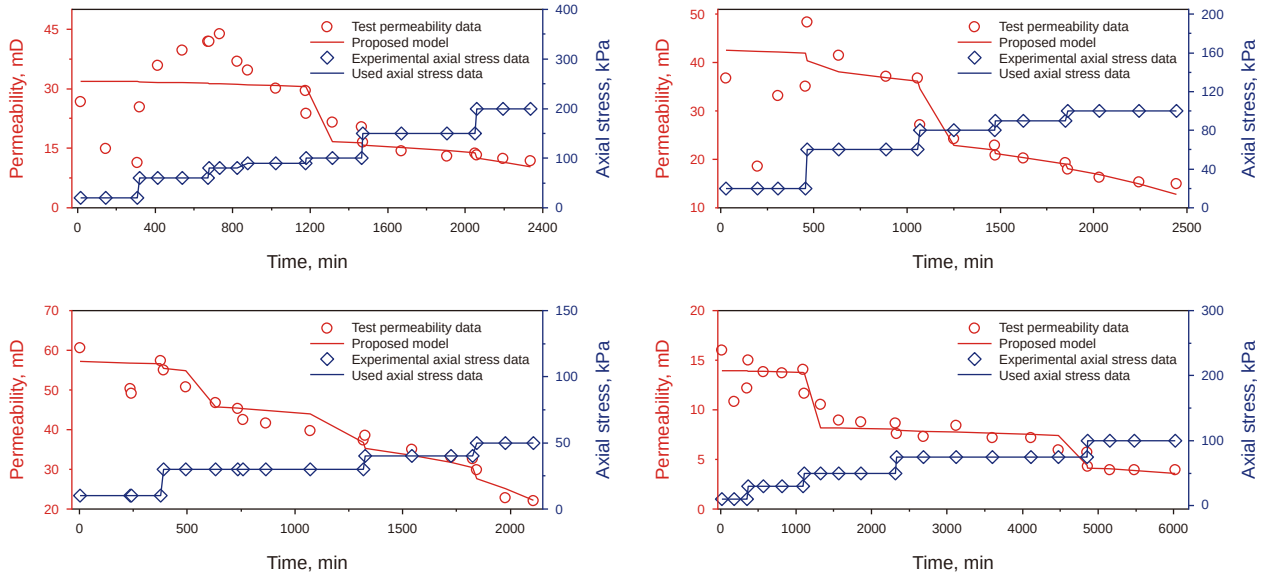


**Fig. 6.** Comparison of predicted permeability with experimental data under different stresses: **(a)** $\sigma_1$ = 20, 60, 80, 90, 100, 150, 200 kPa; **(b)** $\sigma_1$ = 20, 60, 80, 90, 100 kPa; **(c)** $\sigma_1$ = 10, 30, 40, 50 kPa; **(d)** $\sigma_1$ = 10, 30, 50, 75, 100 kPa.

under creep conditions. By performing multiple regression analysis on these six factors, the following empirical equation with a correlation coefficient of 0.992 is obtained.

$$=10.014+0.071\ +\ \ ^{2.5}+13.701\alpha-10.236\ \ +\beta^{1.5}-0.444\sigma_1 \tag{18}$$

*3 3*

In this work, a creep permeability model for hydrate-bearing sediments (HBS) is developed, taking into account the degree of non-uniform particle distribution, particle shape, pore structure, hydrate saturation and hydrate pore morphology. The proposed model represents sediment particles as ellipsoids, which more

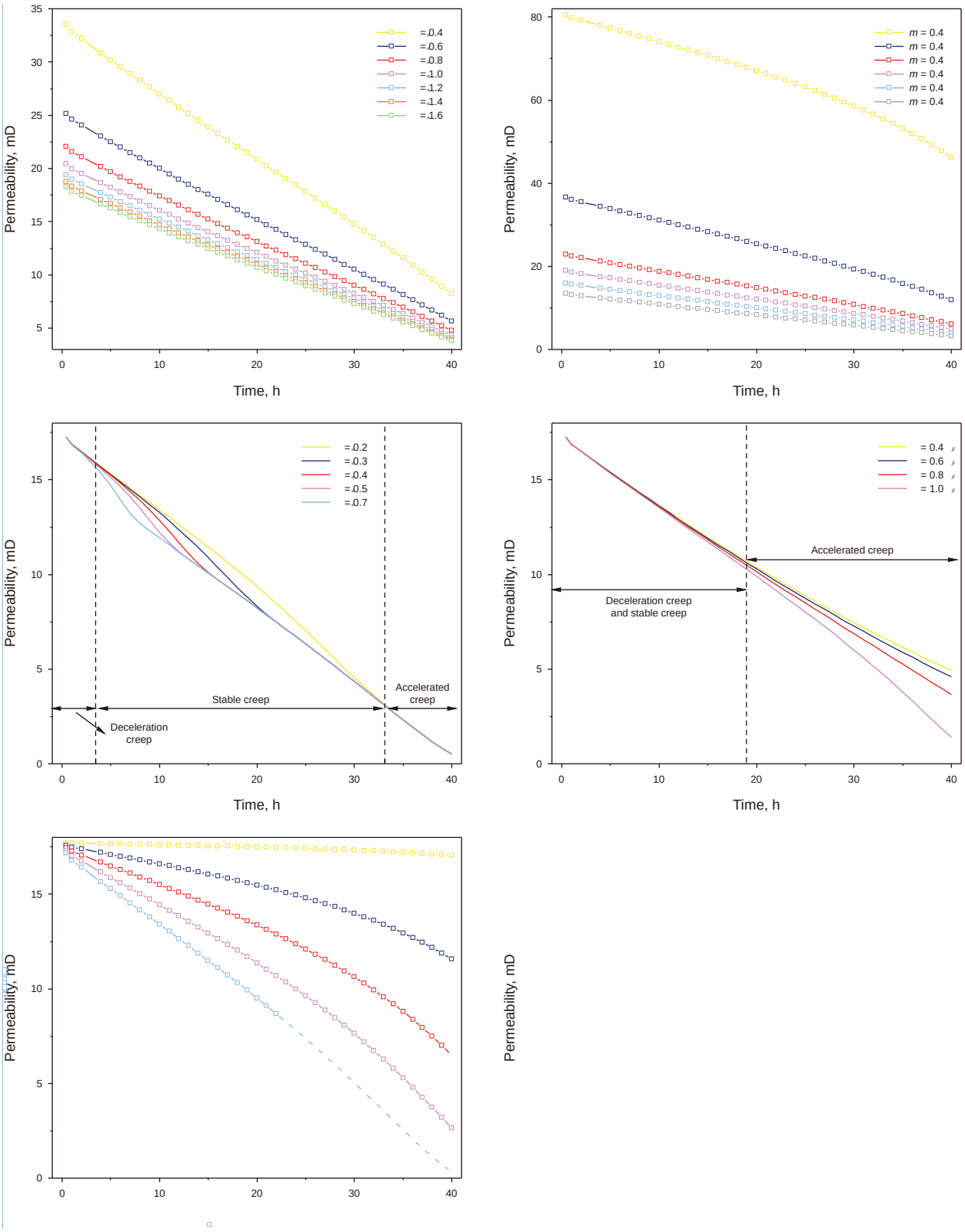


**Fig. 9.** Impact of axial stress, non-uniform parameter, dimensionless creep parameters, and related damage parameters on permeability: **(a)** Ellipsoidal particle aspect ratio $\alpha$; **(b)** Non-uniform parameter ; **(c)** Dimensionless creep parameter ; **(d)** Related damage parameter $\beta$; and **(e)** axial stress $\sigma_1$; **(f)** Aspect ratio $\alpha$ and non-uniform parameter .

closely resemble natural grain morphology than traditional spherical approximations (Song et al., 2024), thereby providing a more physically realistic representation. Moreover, the proposed model employs non-uniform parameters and offset angles to characterize the non-uniform distribution of sediment particles, which more accurately reflects the real characteristics of the reservoir. Additionally, the proposed model comprehensively considers other factors such as pore structure, hydrate saturation, and hydrate pore morphology, which enables it to more accurately capture the permeability evolution of HBS under various loading conditions compared to former models. Therefore, during the long-term exploitation of natural gas hydrates, the permeability model established in this study can be used to accurately predict the dynamic evolution of permeability under creep, thereby optimizing key mining parameters (such as well spacing and depressurization rate) to effectively avoid engineering risks such as wellbore instability and formation sand production caused by sudden changes in permeability (Li et al., 2025). Additionally, the model can analyze the evolution characteristics

## Nomenclature

| | |
|---|---|
| | Creep parameter (dimensionless) |
| 1 | Long axes of ellipsoidal particles, μm |
| 2 | Short axes of ellipsoidal particles, μm |
| | Cross-sectional area of REV, $cm^2$ |
| 0 | Initial center-to-center horizontal distance of two adjacent particles, μm |
| | Center-to-center horizontal distance of two adjacent particles, μm |
| 0 | Initial center-to-center distance of two adjacent particles perpendicular to the flow direction, μm |
| | Circumference of the ellipse, μm |
| f0 | Initial pore fractal dimension (dimensionless) |
| f | Pore fractal dimension under creep (dimensionless) |
| T | Tortuosity fractal dimension (dimensionless) |
| 0 | Shear modulus for the Hooke element, MPa |
| 1 | Shear modulus of the modified Kelvin element, MPa |
| 2 | Shear modulus of the modified viscoplastic element, MPa |
| 1 | Three-dimensional viscosity coefficient of the modified Kelvin element, MPa□h |
| 2 | Three-dimensional viscosity coefficient of the modified viscoplastic element, MPa□h |
| 0 | Bulk modulus for the Hooke element, MPa |
| PF | Permeability of HBS with PF hydrate, mD |
| GC | Permeability of HBS with GC hydrate, mD |
| | Measurement scale of length, cm |
| | Non-uniform parameter, dimensionless |
| Δ | Pressure drop, MPa |
| | Flow rate of a single pipe, $cm^3/s$ |
| $Q_{PF}$ | Total flow through the cross-section of the REV with PF hydrate, $cm^3/s$ |
| $Q_{GC}$ | Total flow through the cross-section of the REV with GC hydrate, $cm^3/s$ |
| max0 | Initial maximum pore radius of HBS, μm |
| max | Maximun pore radius of HBS under creep, μm |
| min0 | Initial minimum pore radius of HBS, μm |
| min | Minimum pore radius of HBS under creep, μm |
| 0 | Initial radius of the spherical particle, μm |
| PF | Pore radius with PF hydrate, μm |
| GC | Pore radius with GC hydrate, μm |
| $S_{h0}$ | Initial hydrate saturation of HBS (dimensionless) |
| $S_h$ | Hydrate saturation of HBS under creep (dimensionless) |
| | Creep duration, h |
| 1 | Damage threshold time, h |
| b0 | Initial apparent volume, $cm^3$ |
| b | Apparent volume under creep, $cm^3$ |
| p0 | Initial pore volume, $cm^3$ |
| p | Pore volume under creep, $cm^3$ |
| Δ p | Pore volume of change, $cm^3$ |
| $\alpha$ | Aspect ratio of the ellipsoidal particles (dimensionless) |
| $\beta$ | Damage-related parameter (dimensionless) |
| $\gamma$ | Transitional hydrate saturaton (dimensionless) |
| $\sigma_1$ | The first principal stress, MPa |
| $\sigma_2$ | The second principal stress, MPa |
| $\sigma_3$ | The third principal stress, MPa |
| $\sigma_s$ | Long-term strength, MPa |
| $\varepsilon_v$ | Volumetric strain (dimensionless) |
| $\theta$ | Offset angle, ° |
| $\tau$ | Average tortuosity (dimensionless) |
| $\lambda$ | Pore size of HBS, μm |
| $\lambda_{min}$ | Minimum pore size of HBS, μm |
| $\lambda_{max}$ | Maximum pore size of HBS, μm |
| $\varphi$ | Porosity of HBS under creep (dimensionless) |
| $\varphi_0$ | Initial porosity of HBS (dimensionless) |
| $\varphi_e$ | Initial effective porosity of HBS (dimensionless) |
| $\mu$ | Fluid dynamic viscosity, Pa□s |
| $\eta$ | Evolutional direction of hydrate pore morphology (dimensionless) |

## Appendix A. Derivation of average tortuosity $\tau$

In this study, the average tortuosity model for hydrate-bearing sediments (HBS) with non-uniform particle distribution is derived based on the model by Peng et al. (2024) under the following assumptions: (I) all particles are identical ellipsoids, with no overlap between particles; (II) the fluid within the HBS is a Newtonian fluid in a laminar flow state. As depicted in Fig. A1(a), the smallest unit of the particle arrangement is represented by yellow lines, with fluid flowing parallel from left to right through adjacent particles within the unit (the red lines represent the fluid paths). Due to the symmetry of the unit structure, a quadrilateral outlined by black dashed lines is used as the calculation model for the average tortuosity, as shown in the enlarged view in Fig. A1(b).

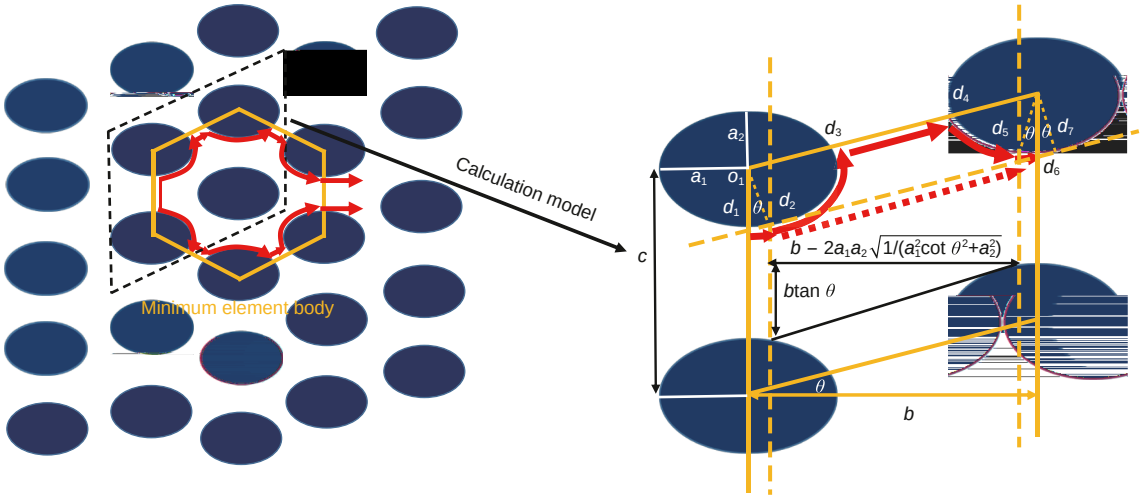


**Fig. A1.** Schematic diagram of ellipsoidal sediment particle arrangement in HBS: **(a)** Particle position arrangement with a given and $\theta$; **(b)** The geometric relationship between adiacent particles and assumed flow paths in pore space.

As shown in Fig. A1(b), the aspect ratio of the ellipsoidal particles is obtained as $\alpha = \frac{-2}{1}$ (A1)

where $\alpha$ denotes the aspect ratio of the ellipsoidal particles, $_1$ and $_2$ are the long and short axes of ellipsoidal particles, respectively.

Regardless of the shape used to represent the sediment particles, the initial porosity of the HBS remains constant, thus the porosity calculated using ellipsoidal sediment particles is equal to that calculated using spherical sediment particles. Therefore, according to the geometric relationship illustrated in Fig. A1(b), the initial porosity of HBS can be expressed as

$$\varphi_0 = \frac{0,0 - \pi\ 0^2}{0,0} = \frac{0,0 - \pi\alpha\ \frac{2}{1}}{0,0} \tag{A2}$$

where $\varphi_0$ denotes the initial porosity of HBS, $_0$ is the initial center-to-center horizontal distance of two adjacent particles in the flow direction, $,_0$ represents the initial center-to-center distance of two adjacent particles perpendicular to the flow direction, $_0$ is the initial radius of the spherical particle. By simplifying Eq. (A2), the following relation can be given as

$$\frac{1}{0} = \sqrt{\frac{(1-\varphi_0)}{\alpha\pi}} \tag{A3}$$

where  represents non-uniform parameter, which can be calculated by $_0/,_0$. Parameter  characterizes the ratio of the horizontal distance to the vertical distance between adjacent sediment particles. The value of  varies with different types of sediments (Zhang et al., 2024a), when  takes different values, the relative positions of sediment particles change.

As shown in Fig. A1(b), $_1$ is the center of the ellipse, $,_1$, $,_3$, $,_4$ and $,_6$ are the intersection points of the quadrilateral formed at the centers of the four ellipses and the four ellipses respectively, $,_2$ and $,_7$ are the tangent points of the common tangent lines to two laterally adjacent ellipses, $,_5$ is symmetric to $,_6$. Since the fluid is in laminar flow, the middle region is divided into the longest path $\overset{\frown}{,_2,_3} + \overline{,_3,_4} + \overset{\frown}{,_4,_5}$, and shortest path $\overline{,_2,_5}$ (Fig. A1(b)), thus the flow path in this region should be represented by the average value, with the typical flow length being $_0$.

Based on the geometry of the ellipse, the circumference of the ellipse and the distances from the center of the ellipse to points $,_2$, $,_3$ on the ellipse are obtained as

$$= 2\pi\ _2 + 4(\ _1 - \ _2) \tag{A4}$$

$$\overline{1,3} = \ _1\ _2\sqrt{\frac{1}{\frac{2}{1}\sin\theta^2 + \frac{2}{2}\cos\theta^2}} \tag{A5}$$

$$\overline{1,2} = \ _1\ _2\sqrt{\frac{1}{\frac{2}{1}\cos\theta^2 + \frac{2}{2}\sin\theta^2}} \tag{A6}$$

where  represents the circumference of the ellipse, $\theta$ represents the offset angle, $\overline{1,2}$ and $\overline{1,3}$ represent the distances from the center of the ellipse to points $,_2$, $,_3$ on the ellipse, respectively.

The elliptic arc $\overset{\frown}{,_1,_2}$ and $\overset{\frown}{,_5,_6}$ are approximated by the length of the arc, which are

$$\overset{\frown}{,_1,_2} = \overset{\frown}{,_5,_6} \approx \ _2\theta \tag{A7}$$

where $\overset{\frown}{,_1,_2}$ and $\overset{\frown}{,_5,_6}$ are the length of elliptic arcare, respectively.

The longest and shortest paths through the pore space of the fluid in the middle region when the typical flow length being $_0$ can be written as

$$_{1,\max} = \frac{1}{2}\left(\overset{\frown}{,_2,_3} + \overline{,_3,_4} + \overset{\frown}{,_4,_5} + \overline{,_2,_5}\right) + \overset{\frown}{,_1,_2} + \overset{\frown}{,_5,_6} = \frac{1}{2}\left[\pi\ _2 + 2(\ _1 - \ _2) - 2\ _2\theta + \frac{0}{\cos\theta} - 2\ _1\ _2\sqrt{\frac{1}{\frac{2}{1}\sin\theta^2 + \frac{2}{2}\cos\theta^2}} + \sqrt{(\ _0\tan\theta)^2 + \left(\ _0 - 2\ _1\ _2\sqrt{\frac{1}{\frac{2}{1}\cot\theta^2 + \frac{2}{2}}}\right)^2}\right] + 2\ _2\theta \tag{A8}$$

$$_{1,\min} = \sqrt{(\ _0\tan\theta)^2 + \left(\ _0 - 2\ _1\ _2\sqrt{\frac{1}{\frac{2}{1}\cot\theta^2 + \frac{2}{2}}}\right)^2} + 2\ _2\theta \tag{A9}$$

where $_{1,\max}$ and $_{1,\min}$ denote the longest and shortest flow paths when the typical flow length being $_0$, respectively.

By combining Eq. (A8) and Eq. (A9), the average path of the fluid is obtained as

$$\bar{}_1 = \frac{_{1,\max} + \ _{1,\min}}{2} = \left\{\frac{3}{4}\left[\sqrt{(\ _0\tan\theta)^2 + \left(\ _0 - 2\ _1\ _2\sqrt{\frac{1}{\frac{2}{1}\cot\theta^2 + \frac{2}{2}}}\right)^2}\right] + \frac{1}{4}\left[\pi\ _2 + 2(\ _1 - \ _2) - 2\ _2\theta + \frac{0}{\cos\theta} - 2\ _1\ _2\sqrt{\frac{1}{\frac{2}{1}\sin\theta^2 + \frac{2}{2}\cos\theta^2}}\right] + 2\ _2\theta\right\} \tag{A10}$$

where $\bar{}_1$ is the average flow path when the typical flow length being $_0$.

Therefore, the tortuosity $\tau_1$ can be calculated as

$$\tau_1 = \frac{\bar{}_1}{0} \tag{A11}$$

where $\tau_1$ is the tortuosity when the typical flow length being $_0$.

According to the model of Peng et al. (2024), if only the middle region is available for flow, the typical flow length becomes $_0 - 2\ _1$, and the tortuosity of HBS should be calculated using the average tortuosity. The longest and shortest paths in the pore space of the fluid can be obtained as

$$_{2,\max} = \frac{1}{2}\left(\overset{\frown}{,_2,_3} + \overline{,_3,_4} + \overset{\frown}{,_4,_5} + \overline{,_2,_5}\right) + \overset{\frown}{,_1,_2} + \overset{\frown}{,_5,_6} = \frac{1}{2}\left[\pi\ _2 + 2(\ _1 - \ _2) - 2\ _2\theta + \frac{0}{\cos\theta} - 2\ _1\ _2\sqrt{\frac{1}{\frac{2}{1}\sin\theta^2 + \frac{2}{2}\cos\theta^2}} + \sqrt{(\ _0\tan\theta)^2 + \left(\ _0 - 2\ _1\ _2\sqrt{\frac{1}{\frac{2}{1}\cot\theta^2 + \frac{2}{2}}}\right)^2}\right] \tag{A12}$$

$$_{2,\min} = \sqrt{\left(\ _0 \tan\theta\right)^2 + \left(\ _0 - 2\ _1\ _2\sqrt{\frac{1}{\frac{2}{1}\cot\theta^2 + \ \frac{2}{2}}}\right)^2} \tag{A13}$$

where $_{2,\max}$ and $_{2,\min}$ denote the longest and shortest flow paths when the typical flow length being $_0 - 2\ _1$, respectively.

Then the average path of the fluid can be determined by combining Eq. (A12) and Eq. (A13), which is

$$\begin{aligned}\bar{}_2 &= \frac{_{2,\max} + \ _{2,\min}}{2} \\ &= \left\{\begin{array}{l} \frac{3}{4}\left[\sqrt{\left(\ _0 \tan\theta\right)^2 + \left(\ _0 - 2\ _1\ _2\sqrt{\frac{1}{\frac{2}{1}\cot\theta^2 + \ \frac{2}{2}}}\right)^2}\right] \\ +\frac{1}{4}\left[\begin{array}{l}\pi\ _2 + 2(\ _1 - \ _2) - 2\ _2\theta + \frac{_0}{\cos\theta} \\ -2\ _1\ _2\sqrt{\frac{1}{\frac{2}{1}\sin\theta^2 + \ \frac{2}{2}\cos\theta^2}}\end{array}\right]\end{array}\right\}\end{aligned} \tag{A14}$$

where $\bar{}_2$ represents the average flow path when the typical flow length being $_0 - 2\ _1$.

The tortuosity $\tau_2$ can be determined by

$$\tau_2 = \frac{\overline{\ \ _2}}{_0 - 2\ _1} \tag{A15}$$

where $\tau_2$ is the tortuosity when the typical flow length being $_0 - 2\ _1$.

Finally, the tortuosity of the HBS composed of ellipsoidal particles can be obtained by averaging Eqs. (A11) and (A15)

$$\tau_{\text{ellipsoid}} = \frac{1}{2}\left(\begin{array}{l}\frac{1}{4}\left[1 + \frac{1}{1 - 2\sqrt{\alpha}\ \ \frac{1}{_0}}\right]\left[\begin{array}{l}\left(\pi\sqrt{\alpha}\ - 2\theta - 2\sqrt{\frac{\alpha}{\sin\theta^2 + (\alpha\cos\theta)^2}}\right)\alpha\frac{1}{_0} \\ +2(1-\alpha)\sqrt{\alpha}\ \ \frac{1}{_0} + \frac{1}{\cos\theta}\end{array}\right] + \\ \frac{3}{4}\left[1 + \frac{1}{1 - 2\sqrt{\alpha}\ \ \frac{1}{_0}}\right]\sqrt{(\tan\theta)^2 + \left(1 - 2\frac{1}{_0}\sqrt{\frac{\alpha^3}{(\cot\theta)^2 + \alpha^2}}\right)^2} + 2\alpha\frac{1}{_0}\theta\end{array}\right) \tag{A16}$$

where $\tau_{\text{ellipsoid}}$ is the average tortuosity of the sediment particles assuming they are ellipsoidal.

When the aspect ratio of the ellipsoidal particle is 1 (i.e., $\alpha = 1$, $_1 = \ _2 = \ _0$), the ellipsoidal particles transform into spherical particles, and the average tortuosity calculated using Eq. (A16) is equal to that calculated by Peng et al. (2024).

$$\begin{aligned}\tau_{\text{ellipsoid}} &= \tau_{\text{sphere}} \\ &= \frac{1}{2}\left\{\begin{array}{l}\frac{1}{4}\left[1 + \frac{1}{1 - 2\frac{_0}{_0}}\right]\left[\frac{1}{\cos\theta} + (\pi - 2\theta - 2)\frac{_0}{_0}\right] + 2\frac{_0}{_0}\theta \\ +\frac{3}{4}\left[1 + \frac{1}{1 - 2\frac{_0}{_0}}\right]\left[\sqrt{(\tan\theta)^2 + \left(1 - 2\frac{_0}{_0}\sin\theta\right)^2}\right]\end{array}\right\}\end{aligned} \tag{A17}$$

where $\tau_{\text{sphere}}$ is the average tortuosity of the sediment particles assuming they are spherical.

By combining Eqs. (A3) and (A16), the average tortuosity of HBS under creep conditions can be obtained by

$$\tau = \frac{1}{8}\left[1 + \frac{1}{1 - \sqrt{\frac{4\ \ (1-\varphi)}{\pi}}}\right]\left[\begin{array}{l}\left(\pi\sqrt{\alpha}\ - 2\theta - \sqrt{\frac{4\alpha}{\sin\theta^2 + (\alpha\cos\theta)^2}}\right)\sqrt{\frac{\alpha\ \ (1-\varphi)}{\pi}} \\ +(1-\alpha)\sqrt{\frac{4\ \ (1-\varphi)}{\pi}} + \frac{1}{\cos\theta}\end{array}\right] +$$

$$\frac{3}{8}\left[1 + \frac{1}{1 - \overline{\qquad}}\right)\left(\rfloor/^{\lceil}\right)\left(\rfloor/^{\lceil}\right.$$

where $\tau$ represents the average tortuosity of HBS during creep, $\varphi$ is the porosity of HBS during creep.

## Appendix B. Fractal characteristics of hydrate-bearing sediments

Since the pore structure of HBS satisfies fractal characteristics, when the Euclidean dimension is 2, the initial pore fractal dimension $_{f0}$ is determined by (Yu and Cheng, 2002; Lei et al., 2019)

$$_{f0} = 2 - \frac{\ln \varphi_0}{\ln(\ _{min0}/\ _{max0})} \quad \text{(B1)}$$

where $_{f0}$ is the initial pore fractal dimension, $_{max0}$ and $_{min0}$ are the initial maximum and minimum pore radius of HBS respectively.

The tortuosity fractal dimension is calculated by (Peng et al., 2024)

$$_T = 1 + \frac{\ln\left\{\left[\tau\left(\ _f + \ _T - 1\right)\right]/\ _f\right\}}{\ln(\ /\lambda_{min})} \quad \text{(B2)}$$

where $_T$ is the tortuosity fractal dimension, $\lambda_{min}$ is the minimum pore size of HBS, $\tau$ is the average tortuosity of HBS during creep.

The actual length $_t$ of the capillary is calculated by

$$_t = \lambda^{1-\ _T\ \ _T} \quad \text{(B3)}$$

Based on Yu (2008), the scaling relationship of the cumulative pore number can be described as

$$(\lambda) = \left(\frac{\lambda_{max}}{\lambda}\right)^{\ _f} \quad \text{(B4)}$$

where denotes cumulative population of pores, $\lambda_{max}$ is the maximum pore size of HBS. By taking the derivative of Eq. (B4)

$$-\mathrm{d}\ \ = \ _f\lambda_{max}^{\ f}\lambda^{-(\ _f+1)}\mathrm{d}\lambda \quad \text{(B5)}$$

## References


Bhade, P., Phirani, J., 2015. Gas production from layered methane hydrate reservoirs. Energy 82, 686–696. https://doi.org/10.1016/j.energy.2015.01.077.

Cai, J.C., Xia, Y.X., Lu, C., Hang, B., Zou, S.M., 2020. Creeping microstructure and fractal permeability model of natural gas hydrate reservoir. Mar. Petrol. Geol. 115, 104282. https://doi.org/10.1016/j.marpetgeo.2020.104282.

Chen, M.T., Li, Y.L., Zhang, Y.J., Qi, M.H., Wu, N.Y., 2023. Recent advances in creep behaviors characterization for hydrate-bearing sediment. Renew. Sustain. Energy Rev. 183, 113434. https://doi.org/10.1016/j.rser.2023.113434.

Cheng, F.B., Wu, Z.R., Sun, X., Shen, S., Wu, P., Liu, W.G., Chen, B.B., Liu, X.J., Li, Y.H., 2023. Compression-induced dynamic change in effective permeability of hydrate-bearing sediments during hydrate dissociation by depressurization. Energy 264, 126137. https://doi.org/10.1016/j.energy.2022.126137.

Chuvilin, E., Grebenkin, Sergey, Zhmaev, M., 2025. Gas permeability of frozen and hydrate-bearing sediments: experimental evidence. Int. J. Geotech. Eng. 19, 276–286. https://doi.org/10.1080/19386362.2025.2492100.

Danesh, N.N., Chen, Z.W., Aminossadati, S.M., Kizil, M.S., Pan, Z.J., Connell, L.D., 2016. Impact of creep on the evolution of coal permeability and gas drainage performance. J. Nat. Gas Sci. Eng. 33, 469–482. https://doi.org/10.1016/j.jngse.2016.05.033.

Du, P.B., Zhao, C.T., Peng, P., Gao, T., Huang, T., 2020. Fractal characterization of permeability prediction model in hydrate-bearing porous media. Chem. Eng. Sci. 218, 115576. https://doi.org/10.1016/j.ces.2020.115576.

Gajanayake, S.M., Gamage, R.P., Li, X.S., Huppert, H., 2023. Natural gas hydrates – insights into a paradigm-shifting energy resource. Energy Rev. 2, 100013. https://doi.org/10.1016/j.enrev.2022.100013.

Gao, X.W., Lei, G., Zhao, Y.J., Liao, Q.Z., Ning, F.L., 2024. A novel theoretical method for upscaling permeability in hydrate-bearing sediments. Water Resour. Res. 60, e2024WR037729. https://doi.org/10.1029/2024WR037729.

Gan, B., Li, Zhandong, Huo, W., Zhang, Y., Li, Zhong, Fan, R., Zhang, H., Xu, Y., He, Y., 2025a. Phase transitions of $CH_4$ hydrates in mud-bearing sediments with oceanic laminar distribution: mechanical response and stabilization-type evolution. Fuel 380, 133185. https://doi.org/10.1016/j.fuel.2024.133185.

Gan, B., Li, Zhandong, Zhang, H., Zhang, Y., Huo, W., Li, Zhong, Xu, Y., Li, Y., 2025b. Optimizing hydrate extraction: balancing stability and production efficiency. Fuel 384, 134088. https://doi.org/10.1016/j.fuel.2024.134088.

Guo, Z.H., Vu, P.N.H., Hussain, F., 2018. A laboratory study of the effect of creep and fines migration on coal permeability during single-phase flow. Int. J. Coal Geol. 200, 61–76. https://doi.org/10.1016/j.coal.2018.10.009.

Hafez, A., Liu, Q., Finkbeiner, T., Alouhali, R.A., Moellendick, T.E., Santamarina, J.C., 2021. The effect of particle shape on discharge and clogging. Sci. Rep. 11, 3309. https://doi.org/10.1038/s41598-021-82744-w.

Hu, Q.B., Li, Y.L., Wu, N.Y., Sun, J.X., Chen, Q., Sun, X.F., 2023. Study on creep behaviors and nonlinear creep constitutive model for sandy hydrate-bearing sediments. Ocean Eng. 288, 115717. https://doi.org/10.1016/j.oceaneng.2023.115717.

Hu, Q., Yin, Z., Dano, C., Hicher, P.-Y., 2011. A constitutive model for granular materials considering grain breakage. Sci. China Technol. Sci. 54, 2188–2196. https://doi.org/10.1007/s11431-011-4491-0.

Katagiri, J., Konno, Y., Yoneda, J., Tenma, N., 2017. Pore-scale modeling of flow in particle packs containing grain-coating and pore-filling hydrates: verification of a Kozeny–Carman-based permeability reduction model. J. Nat. Gas Sci. Eng. 45, 537–551. https://doi.org/10.1016/j.jngse.2017.06.019.

Kerimov, A., Mavko, G., Mukerji, T., Dvorkin, J., Al Ibrahim, M.A., 2018. The influence of convex particles' irregular shape and varying size on porosity, permeability, and bulk elastic modulus of granular porous media: insights from numerical simulations. J. Geophys. Res. Solid Earth 123, 10563–10582. https://doi.org/10.1029/2018JB016031.

Kou, X., Feng, J.C., Li, X.S., Wang, Y., Chen, Z.Y., 2022. Formation mechanism of heterogeneous hydrate-bearing sediments. Appl. Energy 326, 119931. https://doi.org/10.1016/j.apenergy.2022.119931.

Kvamme, B., 2021. Kinetics of hydrate formation, dissociation and reformation. Chem. Thermodyn. Therm. Anal. 1–2,. https://doi.org/16/

hydrate reorganization. Chem. Eng. J. 477, 146973. https://doi.org/10.1016/j.cej.2023.146973.
Liao, D., Wang, S., Zhang, C., 2024. A hypoplastic model for crushable sand under a wide range of stress levels. Acta Geotech 19, 5465–5480. https://doi.org/10.1007/s11440-024-02230-1.
Lin, Z.Z., Dong, H.M., Pan, H.P., Sun, J.M., Fang, H., Wang, X.J., 2019. Study on the equivalence between gas hydrate digital rocks and hydrate rock physical models. J. Pet. Sci. Eng. 181, 106241. https://doi.org/10.1016/j.petrol.2019.106241.
Liu, J.W., Li, X.S., 2021. Recent advances on natural gas hydrate exploration and development in the South China Sea. Energy Fuel 35, 7528–7552. https://doi.org/10.1021/acs.energyfuels.1c00494.
Liu, L.L., Dai, S., Ning, F.L., Cai, J.C., Liu, C.L., Wu, N.Y., 2019. Fractal characteristics of unsaturated sands – implications to relative permeability in hydrate-bearing sediments. J. Nat. Gas Sci. Eng. 66, 11–17. https://doi.org/10.1016/j.jngse.2019.03.019.
Liu, T., Wu, P., Lu, Q.Y., Li, Y.H., Song, Y.C., 2024. Creep and wave velocity characterization on anisotropic consolidated methane hydrate sediments of the South China Sea. Energy Fuel 38, 16416–16425. https://doi.org/10.1021/acs.energyfuels.4c02845.
Liu, X.L., Li, D.J., Han, C., 2020. A nonlinear damage creep model for sandstone based on fractional theory. Arab. J. Geosci. 13, 246. https://doi.org/10.1007/s12517-020-5215-1.
Liu, Y.F., Liu, Y.T., Sun, L., Liu, J., 2016. Multiscale fractal characterization of hierarchical heterogeneity in sandstone reservoirs. Fractals-complex geom. Patterns Scaling Nat. Soc. 24, 1650032. https://doi.org/10.1142/S0218348X16500328.
Liu, Y.F., Jeng, D.S., 2019. Pore scale study of the influence of particle geometry on soil permeability. Adv. Water Resour. 129, 232–249. https://doi.org/10.1016/j.advwatres.2019.05.024.
Lu, C., Xia, Y.X., Qin, X.W., Ma, C., Bian, H., Xing, D.H., Lu, H.F., 2022. Micro- and nanoscale pore structure characterization and mineral composition analysis of clayey-silt hydrate reservoir in South China Sea. Geofluids 2022, 2837193. https://doi.org/10.1155/2022/2837193.
Lu, C., Xia,.X.,